Folded micro-threads: Role of viscosity and interfacial tension

Thomas Cubaud,[a] Bibin M. Jose, and Samira Darvishi
Department of Mechanical Engineering, Stony Brook University, Stony Brook, New York 11794, USA

(Received 15 October 2010; accepted 11 March 2011; published online 13 April 2011)

The shape and evolution of periodically folded threads are experimentally examined in a microfluidic network. The fluidic system is designed for the production and lubricated transport of very uniform folds. To investigate the influence of viscosity and interfacial tension on buckling deformations, multiphase flows are scrutinized using both miscible and immiscible fluid pairs. The parameters used to analyze folding morphologies include thread diameter, arc-length, fold amplitude, and wavelength. When fluids are immiscible, the onset of viscous folding is characterized as a function of the capillary number and the phenomenon of "capillary unfolding" where a corrugated thread straightens along the flow direction is demonstrated. The spatial transition from folding to coiling-like flow behavior of high-viscosity capillary threads is also shown.
 [doi:10.1063/1.3573383]

I. INTRODUCTION

Interfacial instabilities play an important role in fluid dynamics and multiphase processes. At the small scale, manipulating the shape of fluid interfaces is practical for the generation of bubbles and droplets. Capillary surfaces find use in a variety of microfluidic applications,[1–5] such as segmented flow of bubbles for enhanced mixing,[6] microreactions in droplets,[7] and tunable optofluidic elements.[8,9] A key feature in these systems is the interplay between flows and microgeometries for passively destabilizing laminar streams and interfaces. Typical multiphase flow instabilities include the Rayleigh–Plateau instability[10–13] between two immiscible fluids, i.e., the breakup of an unstable cylindrical thread into droplets, and the Saffman–Taylor instability[14–16] when a miscible fluid is injected into a quiescent viscosity-differing fluid and forms fingering patterns.

Fluid threads belong to a class of flow structures having common characteristics between miscible and immiscible streams. Recent manipulations of miscible core-annular flows uncovered the possibility to buckle high-viscosity fluid threads in diverging microchannels.[17] For short intervals of time,[18] the elastic-like behavior of slender viscous structures has been investigated in situations as diverse as the viscous catenary,[19,20] conical singularities[21] and rippling instabilities[22,23] of thin viscous sheets, and the buckling of viscous fluid ropes falling onto a surface.[24–31] The shape of viscous folds has also received attention in the context structural geology with focus on phenomena such as ramp faulting[32–34] and subduction.[35,36] Analyses of the mechanism of layer-parallel shortening of viscous sheets embedded in viscous media are sometimes used to estimate the viscosity contrast between layered rocks.[37] In general, systematic laboratory experiments dealing with the flow of high-viscosity fluids at the large scale are difficult to conduct due to the effects of gravity, the need for large amounts of viscous material, and the long time-scale required for reaching steady state.

Here, experiments are carried out in microchannels to probe and manipulate viscous buckling instabilities. This study is motivated by the need for developing methods for the control of high-viscosity fluids in continuous microreactors. Microfluidic devices are advantageous for combining viscous and capillary instabilities and for engineering novel microflow regimes. Previous work on the topic of viscous buckling at the microscale includes the formation of lubricated fluid threads in square microchannels,[38,39] the occurrence of the folding instability in diverging microchannels,[17,40] and the behavior of two-fluid miscible flows in plane microchannels in the presence of a constriction.[41] In the latter case, viscous stratifications can evolve to form a lubricated thread, which buckles downstream from the constriction. The physical origin of the instability is rooted in the presence of an axial compressive stress along the decelerating filament.[42] In practice, the formation of regularly buckled structures in diverging microflows is challenging due to (a) the creation of a slow moving pile, which results from the lubrication failure of large threads on the top and bottom walls, and (b) the secondary folding phenomena (i.e., the folding of a folded thread)[41] for small threads. The difficulty in producing spatially homogeneous structures has precluded the quantitative investigation of the influence of fluid properties on buckling morphologies at the microscale.

A novel model system enabling the production of uniformly folded threads is introduced. The microfluidic network is composed of a diverging channel connected to three channels that are used to study lubricated viscous structures in straight and compact geometries. This method significantly inhibits secondary folding phenomena. Furthermore, we adopt an original experimental methodology that permits a direct comparative study between miscible and immiscible multifluid dynamics.

We first focus on the behavior of miscible fluid threads in a flow regime where diffusion effects are negligible. The evolution of the thread diameter and envelope amplitude of folds is examined for a wide range of viscosity contrasts. Measuring the spatial period of deformed threads permits the

[a]Author to whom correspondence should be addressed. Electronic mail: thomas.cubaud@stonybrook.edu.

classification of fold shapes using a single phase-diagram. The degree of thread corrugation along the flow direction is also characterized during the development of the folding instability.

Capillary threads having significant interfacial tension with the sheath fluid are also examined. The transition from simple dilation to folding flow regimes is revealed based on the capillary number. The envelope amplitude of capillary folds is compared with the miscible fluid case. In particular, as capillary effects tend to reduce interfacial area, we show that, in compact microchannels, threads can unfold along the flow direction. Finally, an intriguing folding to coiling-like transition is reported for very large viscosity contrasts.

II. EXPERIMENTAL SETUP

Using conventional silicon-based microfabrication techniques,[43] we have built a microchannel network made of a silicon slide, which is etched through and sandwiched between two glass plates. The microfluidic module is placed on the top of an inverted microscope equipped with a high-speed camera. The module is illuminated from above using a fiber light bundle and fluids are fed into the channels using high-pressure syringe pumps. Images and movies are analyzed using a combination of FORTRAN routines and IMAGEJ.[44] In this experiment, the fluidic system is composed of four consecutive elements including a focusing section, square channel, diverging channel, and separation region composed of three rectangular channels arranged in parallel [Fig. 1(a)].

The channel height remains constant along the network, $h=250$ μm, and the width of the central channel is $w=417$ μm, which yields a central channel aspect ratio of $w/h=1.66$. The side channel width is $w_s=542$ μm and the distance between the square and the central channel is $L=850$ μm. The mean velocity reduction between these two channels is estimated using mass conservation according to $V_{central}/V_{square} \sim h/(2w_s+w)=1/6$. We seed a single-fluid flow with 2 μm latex beads to visualize the streamlines associated with the diverging sector [Fig. 1(b)]. The flow rates investigated correspond to a Reynolds number Re ranging between 5×10^{-2} and 20. As expected for such low Re, Jeffery–Hamel flows[45–47] are not observed in the diverging channel. The streamline separation points S at the transition between the diverging and the central channel remain fixed in space. The stagnation streamlines correspond to the edge of a virtual stream having a width $\varepsilon/h \sim 0.33$ in the square channel.

A viscous thread is formed in the square channel by focusing a high-viscosity liquid $L1$ having a viscosity η_1 and a flow rate Q_1 in a sheath of a liquid $L2$ having a viscosity η_2 and a total flow rate Q_2. The focusing section and the square microchannel of length $L_c/h=10$ have been designed to generate well-developed threads.[39] In the square microchannel, their diameter ε_0 depends only on the flow rate ratio $\varphi=Q_1/Q_2$ according to $\varepsilon_0/h \approx (\varphi/2)^{1/2}$ when the viscosity contrast $\chi=\eta_1/\eta_2$ is larger than 15.

The system geometry was designed to produce uniformly folded structures made of high-viscosity fluids. The

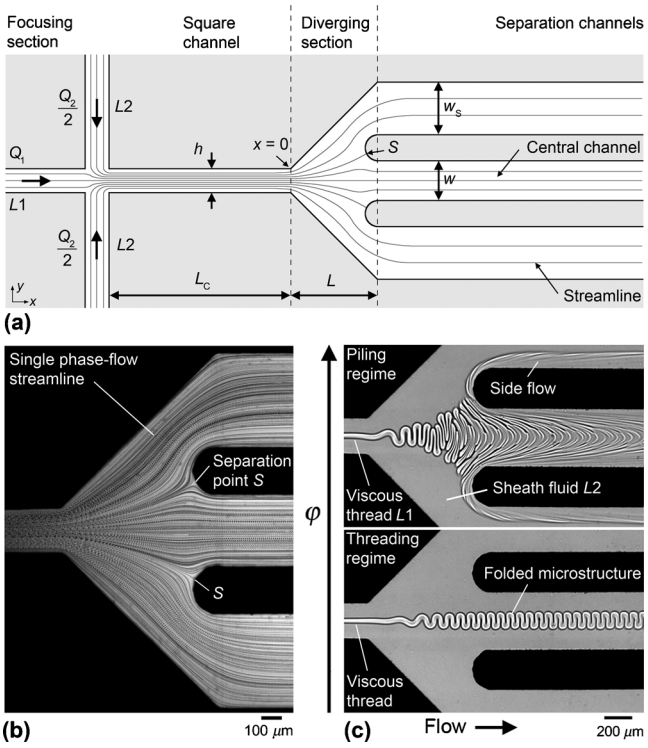

FIG. 1. Formation of uniformly folded threads. (a) Schematics of microchannel design with single-fluid streamlines. (b) Experimental composite micrograph of single-fluid streamlines in the diverging channel. (c) Micrograph of two-fluid flows in separation channels ($L1$: silicone oil, $\eta_1=486$ cP; $L2$: silicone oil, $\eta_2=9.35$ cP); top: fouling of the central channel for a thick thread ($\varphi=8.3\times10^{-2}$); bottom: folding of a thin lubricated thread ($\varphi=5.5\times10^{-2}$).

diverging channel is used to initiate the folding instability and the resulting flow architectures are observed in the central channel. The rectangular observation channel is compact and significantly confines lubricated structures with straight streamlines, which are imposed by the vicinity of the four walls. The "threading regime" occurs for small thread size ε_0 (i.e., for small flow rate ratios φ) and consists of a deformed thread lubricated by the ensheathing fluid $L2$. Another flow pattern, which we name "piling regime," corresponds to large flow rate ratios φ [Fig. 1(c)]. In this case, a thick thread makes effective contact with the walls, fouls the central channel with a slow moving pile, and produces viscous stratifications in the side channels. Here, we focus our attention to small viscous filaments in the threading regime, away from the transition to the piling regime. The folded structures considered in this paper are small compared to the channel dimensions and wall effects are not assumed to perturb flow morphologies.

A sketch of the length scales used to characterize folding morphologies is shown in Fig. 2. Variables include the thread diameter ε and arc-length s, the wavelength of folding λ in the central channel, and the amplitude A of the envelope defined by the thread undulation. As the thread is convected in the external fluid, these quantities vary along the longitudinal coordinate x. The origin $(x,y)=(0,0)$ is set in the middle of the square channel at the transition with the diverging channel. This study focuses on the role of viscosity

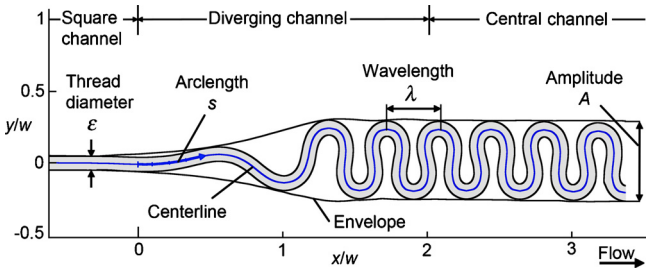

FIG. 2. (Color online) Schematic of a folding thread with geometrical parameters of interest: thread diameter ε, arc-length s, wavelength λ, and envelope amplitude A.

and interfacial tension in the deformation of micro-threads. To experimentally decouple viscous from interfacial tension phenomena, miscible fluid threads are first inspected to characterize purely viscous effects. Second, capillary threads are examined in the presence of interfacial tension γ_{12} between the two fluids and their morphologies are compared with those of miscible fluid threads.

III. MISCIBLE THREADS

Fully miscible threads are made using conventional silicone oils for $L1$ and $L2$. These oils have a dynamic viscosity η that ranges between 0.5 and 9740 cP. Fluid pairs are selected to study the role of a viscosity contrast $\chi=\eta_1/\eta_2$ that spans over nearly three orders of magnitude, between 26 and 19 480. The relationship between the absolute thread viscosity η_1 and the dimensionless viscosity contrast χ is investigated using two matching viscosity contrasts: (a) $\chi=106$ ($\eta_1=486$ and $\eta_2=4.59$ cP) and $\chi=101$ ($\eta_1=9740$ and $\eta_2=96$ cP) and (b) $\chi=592$ ($\eta_1=486$ and $\eta_2=0.82$ cP) and $\chi=512$ ($\eta_1=9740$ and $\eta_2=19$ cP). Although these fluid pairs have different coefficients of diffusion D, which results from the differing molecular weight of each oil,[41] no significant departure in thread morphology is observed for matching χ. Hence, the viscosity contrast χ between the thread and the sheath fluid is assumed to define the effective thread viscosity. Experiments are conducted in the Newtonian flow regime of silicone oils at shear-rates below 10^3 s^{-1}.

Typical folding flow morphologies in the central channel are displayed in Fig. 3. Miscible thread shapes are arranged on a chart of similar envelope amplitudes A for various viscosity ratios χ. Multiphase transport of fluids having a large difference in viscosities is characterized by a disparity between the flow time-scales associated with each fluid. In the case of a high-viscosity thread lubricated by a low-viscosity fluid, balancing shear stresses at the $L1/L2$ interface yields $t_1 \sim \chi t_2$, where t_1 is the thread flow time-scale and t_2 is the sheath fluid flow time-scale. As the thread is swept away in the flow of $L2$, the characteristic time-scale of the experiment t is comparable to the convective time-scale $t \sim t_2$ of the low-viscosity fluid $L2$. As a result, for low χ, the thread exhibits a fluid-like behavior and, in the field of view of the camera, $L1$ appears to "reflows" within the thread. By contrast, for large χ, the thread appears more rigid and exhibits a solid-like behavior. The transition between these two asymptotic regimes and the resulting flow morphologies associated with different χ are quantitatively discussed in Secs. III A–III D.

A. Thread diameter

For low viscosity contrast χ, the thread appreciably swells in the divergence (Fig. 4). To quantify this effect, the thread diameter is measured in the decelerating flow field: $\varepsilon(x=h)=\varepsilon_h$. The relative diameter increase is characterized by the thread "dilation factor" $\sigma=\varepsilon_h/\varepsilon_0-1$, where ε_0 is the initial thread thickness in the square channel. Assuming a linear growth with x in the divergence ($x>0$), the thread diameter can be expressed as

$$\varepsilon = \varepsilon_0(1+\sigma x/h). \tag{1}$$

The dilation factor σ is measured using the minimum intensity in the grayscale profile of a thread to determine ε_0 and ε_h. This method, which allows for enhanced precision, is helpful here because threads are relatively thin. As expected, the ratio $\varepsilon_h/\varepsilon_0$ tends to unity when $\chi \to \infty$ [Fig. 4(d)]. Extrapolating our analysis to a single-phase flow with $\chi=1$ and a divergence having a $\pi/2$ aperture angle, the dilation factor yields $\sigma=2$. In Fig. 4(e), this data point is included in the plot of the dilation factor σ as a function of the viscosity

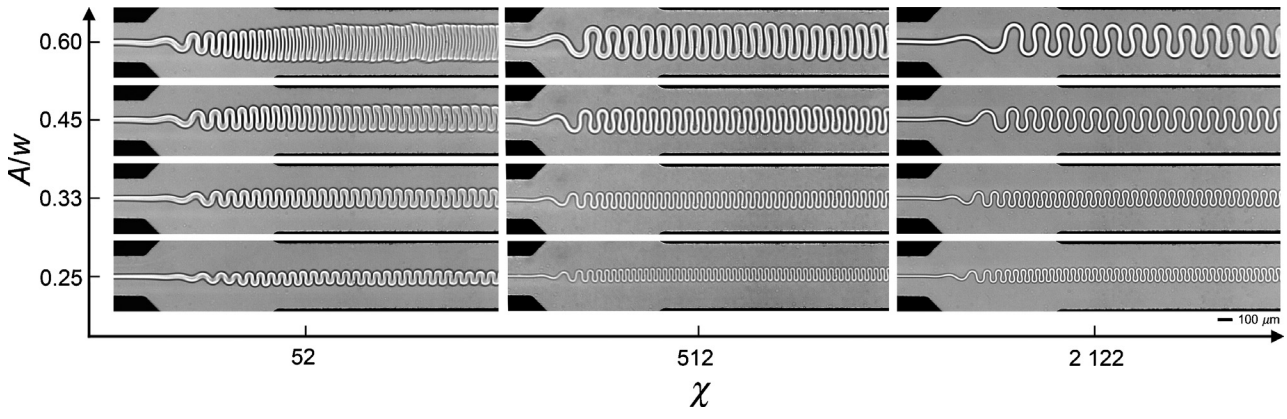

FIG. 3. Chart of steady viscous folds. $\chi=52$, $\varphi^{-1}=10,12,18,20$ (from top to bottom); $\chi=512$, $\varphi^{-1}=17,40,90,150$ (from top to bottom); $\chi=2122$, $\varphi^{-1}=40,80,150,200$ (from top to bottom).

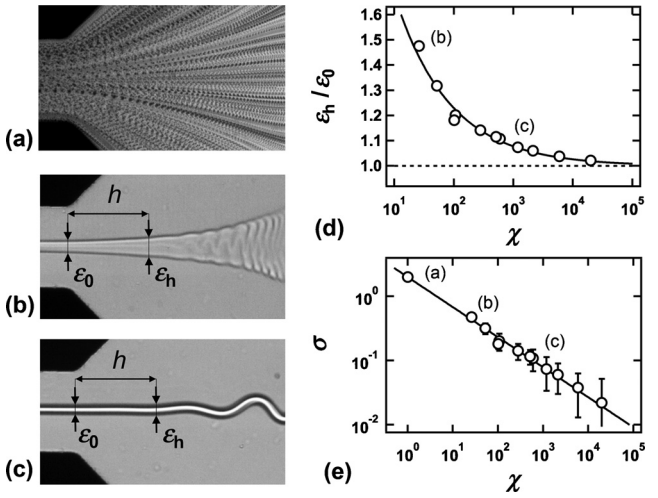

FIG. 4. Dilation of a weakly diffusive thread in a diverging flow field. (a) Single-fluid streamlines in the extensional flow. (b) Low viscosity contrast (χ=26). (c) Large viscosity contrast (χ=1184). (d) Mean evolution of the diameter ratio $\varepsilon_h/\varepsilon_0$ vs viscosity contrast χ. (e) Dilation factor σ (solid line: $\sigma=2\chi^{-0.47}$).

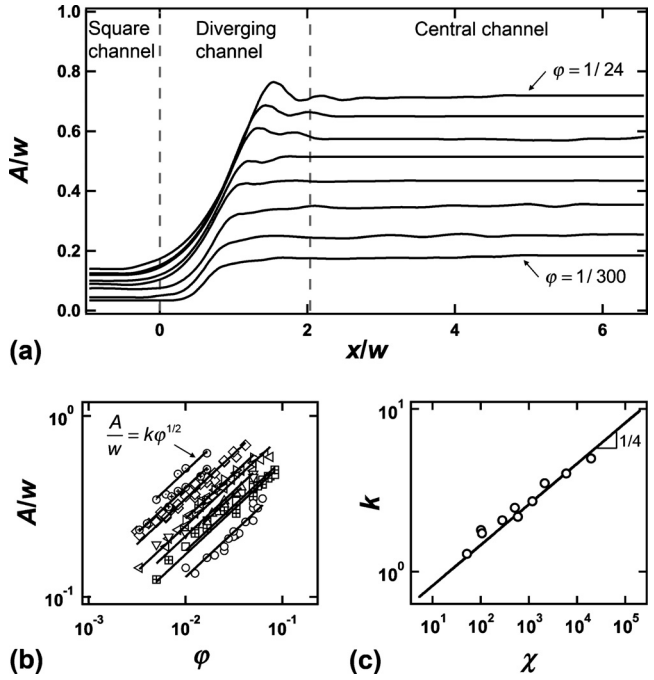

FIG. 5. Envelope amplitude of viscous threads. (a) Spatial evolution of envelope amplitude A/w for various flow rate ratios φ for χ=2122, from top to bottom: φ^{-1}=24,32,40,60,80,100,200,300. (b) Amplitude A/w vs flow rate ratio φ for viscosity contrasts χ=52 (○), 101 (□), 105 (), 279 (△), 512 (◁), 592 (▽), 1184 (▷), 2122 (◇), 5932 (⊗), and 19 480 (⊙), solid lines: $A/w=k\varphi^{1/2}$. (c) Prefactor k vs viscosity contrast χ, solid line: $k=0.46\chi^{1/4}$.

contrast χ and data are well fit with the expression $\sigma=2\chi^{-0.47}$. To our knowledge, the flow of a lubricated thread along a diverging channel is still poorly understood theoretically. Our empirical scaling, however, suggests $\sigma\sim\chi^{-1/2}$ and gives a useful estimate of the thread radial growth in the divergence. For instance, at the entrance of the central channel ($x\approx L$) and in the absence of folding, the thread diameter is expected to increase by a factor of 2 for χ=52, while for χ=1184, the increase is approximately 1.25. For low χ, large thread dilation prohibits significant folding, as shown in Fig. 4(b). The small viscosity contrast χ=26 reported in this graph is not included with data in the remainder of this article due to the difficulty in forming well-developed folded threads for such low χ.

In the central channel, observations indicate that ε remains essentially constant along the flow direction for large χ. By contrast, for low χ, folded microstructures evolve in the straight central channel. The thread diameter characteristically thins in the regions between bends for large amplitude (Fig. 3, χ=52). This modification for low χ, however, is relatively negligible and does not significantly alter thread wavelength and folding amplitude for small folding amplitudes.

B. Envelope amplitude

The evolution of the envelope amplitude A is measured during the folding process from the square channel to the central channel [Fig. 5(a)]. Using edge detection algorithms, the width of the envelope A is extracted from composite images that are constructed using a superposition of pictures taken from high-speed movies. In the square channel, the amplitude corresponds to the thread initial diameter $A\sim\varepsilon_0$ since no folding occurs. Near the diverging channel, thick threads begin to undulate causing a slight increase in A, which is further amplified downstream. In the diverging channel, the amplitude A reaches its final size in the middle of the diverging channel for low φ. For large φ, A attains a maximal value in the diverging channel [Fig. 5(a), φ=1/24]. The existence of this maximum is interpreted as the interplay between the thread locking into a definite shape and the focusing of streamlines from the diverging to the central channel. In the central channel, the amplitude A remains constant regardless of flow rate ratio φ. For a variety of viscosity ratios χ, we measure the stable amplitude A in the central channel as a function of φ [Fig. 5(b)]. Similar to the thread diameter dependence on φ in circular and square channels, $\varepsilon_0/h=(\varphi/2)^{1/2}$, data are well fit with the scaling $A/w=k\varphi^{1/2}$ where k is a function of χ. In the theory associated with the periodic folding of viscous sheets in air,[35,48] the amplitude scales as $A\sim\eta^{1/4}$, where η is the sheet viscosity. In the presence of a viscous environment, we expect a similar scaling for the envelope amplitude $A\sim\chi^{1/4}$, where χ is the viscosity ratio. Therefore, we fit the data with $k=c\chi^{1/4}$ and find good agreement for c=0.46 over nearly three decades in χ [Fig. 5(c)]. Overall, steady miscible fluid threads are experimentally found to follow the relationship

$$A/w = c\chi^{1/4}\varphi^{1/2}, \tag{2}$$

with c being a geometrical constant c=0.46 associated with confinement (i.e., channel aspect ratio).

C. Wavelength

The spatial period of folds λ in the central channel is an important component of the thread deformation geometry. Normalizing both the wavelength λ and the envelope amplitude A with the initial thread diameter ε_0 allows for classi-

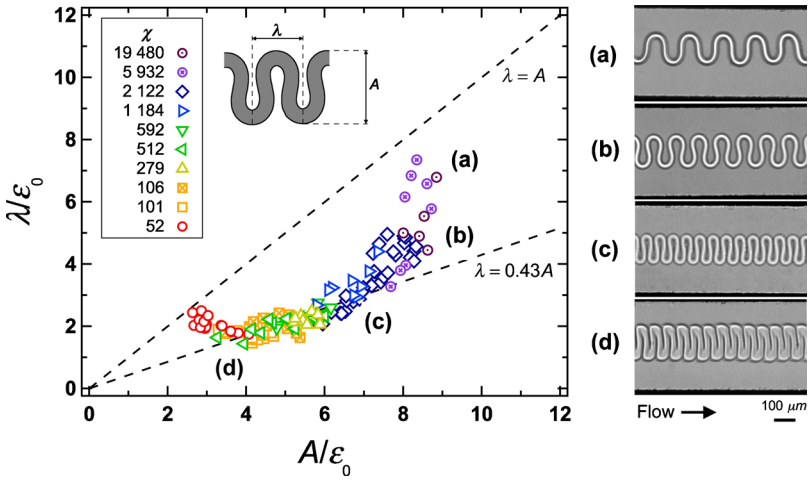

FIG. 6. (Color online) Form of folds diagram. Normalized wavelength λ/ε_0 vs amplitude A/ε_0 with corresponding fold styles, flow rates in μl/min: (a) $\chi=5932$, $Q_1=5$, $Q_2=400$; (b) $\chi=2122$, $Q_1=5$, $Q_2=400$; (c) $\chi=592$, $Q_1=2$, $Q_2=120$; (d) $\chi=52$, $Q_1=10$, $Q_2=120$.

fying fold shapes on a single phase-diagram (Fig. 6). This representation permits the localization of different regions of viscosity contrast χ based on the dimensionless envelope amplitude, since according to Eq. (2) and the scaling for the thread initial diameter, $\varepsilon_0 \sim \varphi^{1/2}$, the normalized amplitude scales as $A/\varepsilon_0 \sim \chi^{1/4}$. Figure 6 captures the essential geometrical features of viscous folds and data collapse into a crescent-shaped curve bounded by the line $\lambda=A$. Although the curve is continuous, three regions of χ are identified. For $\chi \leq 10^2$, the normalized wavelength λ/ε_0 remains nearly constant. For χ ranging between 10^2 and 10^3, the wavelength λ is directly proportional to the amplitude A as indicated by the dashed-line $\lambda=0.43A$. Finally, for $\chi \geq 10^3$, the wavelength λ sharply increases with A. For the intermediate χ regime, a simple scaling suggests $\lambda/\varepsilon_0 \sim \chi^{1/4}$. This result compares qualitatively with the theory of layer-parallel shortening[37] where $\lambda/\varepsilon_0 \sim \chi^{1/3}$. However, a major difference between our experiment and the parallel shortening configuration is the use of a confining geometry and continuous flows, which results in a fixed folding amplitude A. A comprehensive theoretical analysis would provide a more unifying picture on the influence of the viscosity contrast χ on the fold wavelength λ for a variety of situations.

D. Arc-length

Buckling morphologies consist in a strong corrugation of the thread centerline. Periodically folded threads produce packed viscous structures that are translated along the microfluidic network. The degree of thread corrugation is evaluated here using the mean spatial derivative of the thread arc-length ds/dx in the central channel. For a given flow situation, the arc-length $s(x)$ is determined using a series of image-processing filters, such as thresholding, filling the thread central part, and skeletonizing, on sample images taken from experimental movies. Edge detection algorithms are then applied to the resulting thread skeleton to extract its curvilinear abscissa $s(x)$ [Fig. 7(a)]. Since folds can "curl up," $s(x)$ is not necessarily an injective function of x. The mean derivative of s with respect to x, ds/dx, however, is calculated by applying a Loess smoothing filter that produces a bijective function. In Fig. 7(a), this function appears as black while the detected arc-length appears in gray. At the beginning of the diverging channel, the thread is not significantly bent so $s \approx x$. As the thread begins to undulate and fold further downstream, ds/dx increases with x and reaches a saturation value that overall remains constant in the central channel $(x/w > 2)$ [Fig. 7(b)].

The viscous structures observed in the central channel have a homogeneous wavelength λ and amplitude A. In this case, the mean thread corrugation ds/dx is identical to the arc-to-wavelength ratio S/λ. We measure S/λ (i.e., the saturation value of ds/dx in the central channel) for a variety of flow conditions and find that, for low envelope amplitudes $(A/w \leq 0.55)$, this quantity fluctuates around a mean value

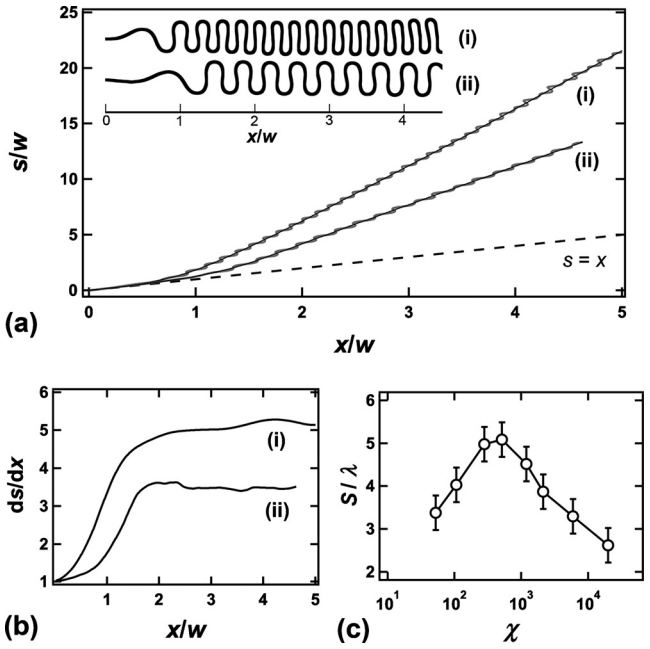

FIG. 7. Arc-length of miscible threads. (a) Spatial evolution of the normalized thread arc-length s/w vs normalized distance from the inlet channel x/w for $A/w \approx 0.55$, flow rate in μL/min: (i) $\chi=512$, $Q_1=3$, $Q_2=50$; (ii) $\chi=2122$, $Q_1=5$, $Q_2=200$. Inset: corresponding thickened skeleton. Dashed line: $s=x$. Solid line: smoothed data from which spatial derivative ds/dx is calculated. (b) Spatial evolution of ds/dx for cases (i) and (ii). (c) Evolution of the arc-to-wavelength ratio S/λ as a function of viscosity contrast χ.

for each viscosity ratio χ [Fig. 7(c)]. The maximum corrugation is experimentally found for moderate χ ranging between 2×10^2 and 10^3. Although structures appear most compact for low χ [Fig. 6(d)], folds are more curled and centerlines are more distorted for moderate χ [Fig. 6(c)]. For large χ, the significant increase in λ results in less corrugated threads [Figs. 6(a) and 6(b)]. This general trend can also be deduced using a rectangular waveform model together with the wavelength measurements. The fold arc-length S is approximated by $S=\lambda+2A_1$, where A_1 is the centerline fold amplitude, i.e., $A_1\approx A-\varepsilon$. For low and moderate χ, data indicate that $\lambda/\varepsilon_0\approx2$. Neglecting variations in the thread radius (i.e., $\varepsilon\approx\varepsilon_0$) yields $S\approx2A$. For low χ, the wavelength λ is relatively independent from A and scales as $\lambda\sim\varepsilon\sim\varphi^{1/2}$. Thus, according to Eq. (2), the arc-to-wavelength ratio is expected to grow with the viscosity contrast such as $S/\lambda\sim\chi^{1/4}$. For moderate χ, data show that $\lambda=0.43A$ and the arc-to-wavelength ratio should remain relatively constant, $S/\lambda\approx4.6$. This value is in relatively good agreement with digitally measured arc-to-wavelength ratios, $S/\lambda\sim5$ [Fig. 7(c)]. For large viscosity ratios, the sharp increase in the wavelength produces smaller S/λ.

Overall, our experimental investigation of the interplay between buckling morphology and microflows shows that thread deformations are paramount for moderate χ. The parameter S/λ provides a simple estimate of the degree of thread packing along the flow. In terms of multiphase flows, the evolution of S/λ is also important for assessing the effective volume fraction $\alpha_1\approx[\pi\varepsilon^2/(4hw)](S/\lambda)$ of the "dispersed phase" (i.e., thread) in the central channel.

IV. IMMISCIBLE THREADS

We now focus on the influence of interfacial tension γ_{12} on the morphology of folded threads. Using the same microchannel module, a series of experiments is conducted using silicone oils (viscosity $\eta_1=194$, 486, 971, and 4865 cP) for $L1$ and ethanol ($\eta_2=1.14$ cP) for $L2$. When immersed in $L2$, a small drop of $L1$ deposited on a glass surface adopts a spherical shape with a contact angle $\theta_{12}\approx180°$, so the thread does not wet the walls. The interfacial tension between silicone oil and ethanol is measured as $\gamma_{12}\approx1.5$ mN/m using the combined capillary rise technique.[49] Steady immiscible threads[38] are formed in the hydrodynamic focusing section when the $L1$ injection capillary number $\mathrm{Ca}_1=Q_1\eta_1/(h^2\gamma_{12})\gg10^{-1}$. In this case, the diameter of capillary threads in the square microchannel obeys the same functional relationship as the one followed by miscible threads: $\varepsilon/h\approx(\varphi/2)^{1/2}$. Therefore, miscible and capillary threads have identical morphology upstream from the diverging channel, which allows for a detailed comparative study.

Figure 8 displays the influence of Ca on the dynamic response of capillary threads to the viscous buckling instability. The reference capillary number $\mathrm{Ca}=\eta_1(Q_1+Q_2)/(h^2\gamma_{12})$ is calculated based on the thread viscosity η_1 and the average multiphase velocity in the square microchannel. It is important to note that Fig. 8 includes Ca calculated for different viscosity contrast χ. The observed morphologies result from the competing effects between the buckling instability, which typically increases the thread surface area, and capillary forces, which tend to decrease the interfacial area. As Ca becomes large, flow patterns resemble those of the purely viscous case with negligible interfacial tension. We identify the regime dominated by interfacial tension for $\mathrm{Ca}<14$ (no folding) and the regime dominated by viscous effects for $\mathrm{Ca}>100$ (strong folding). Intermediate flow regimes are characterized by the rapid "unfolding" of the thread along the central channel.

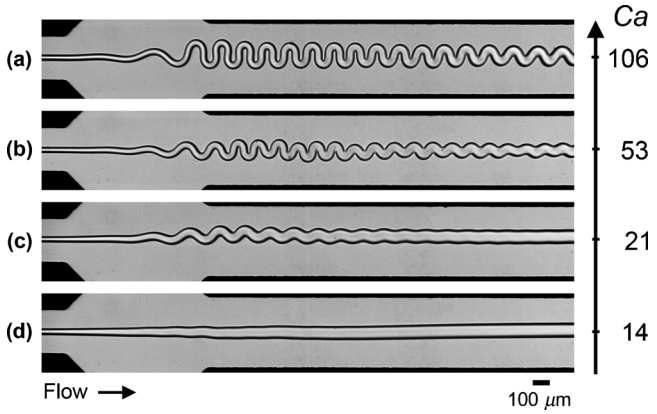

FIG. 8. Onset of folding of a capillary thread. Fixed flow rate ratio $\varphi=0.025$, flow rates in μl/min: (a) $\chi=170$, $Q_1=10$, $Q_2=400$; (b) $\chi=170$, $Q_1=15$, $Q_2=600$; (c) $\chi=425$, $Q_1=15$, $Q_2=600$; (d) $\chi=851$, $Q_1=15$, $Q_2=600$. Capillary numbers Ca are based on the inlet square channel.

A. Capillary envelope amplitude

The spatial evolution of the envelope amplitude A of a folding capillary thread is shown in Fig. 9(a). For a given viscosity contrast χ and a fixed flow rate ratio φ, the effect of capillary forces is twofold: in the diverging channel, the envelope width A decreases with Ca, while in the central channel, A increases with Ca.

In the diverging channel, we find that capillary thread dilation factors σ are only 5% larger than the miscible fluid case that follows the empirical correlation $\sigma\sim2\chi^{-0.47}$. Thus, in the decelerating flow region, thread diameters do not significantly vary between miscible and immiscible fluids. At the entrance of the central channel, $x/w\approx2$, the folding amplitude A, however, reaches a value A_c, which is considerably larger than its miscible counterpart A_m calculated using Eq. (2). For various χ, capillary envelope amplitudes A_c/w are measured as a function of φ [Fig. 9(b)]. Data points are scattered due to variations in the capillary numbers investigated for each fluid pair. For a given χ, fixing the flow rate ratio φ reduces data dispersion and shows the influence of Ca [Fig. 9(c)]. The parameter A_c/A_m tends to unity in a nearly linear fashion as Ca increases. Although the critical capillary number for immiscible/miscible fluid equivalence, i.e., $A_c/A_m=1$, also depends on the flow rate ratio φ, it is estimated as $\mathrm{Ca}\sim150$ for $\chi=851$. We note that as χ or η_1 are changed the amplitude ratio A_c/A_m widely varies. For instance, for $\varphi^{-1}=80$, we find that $A_c/A_m\approx1.17$ for $\mathrm{Ca}=140$ ($\eta_1=971$ cP), while $A_c/A_m\approx1.77$ for $\mathrm{Ca}=700$ (η_1

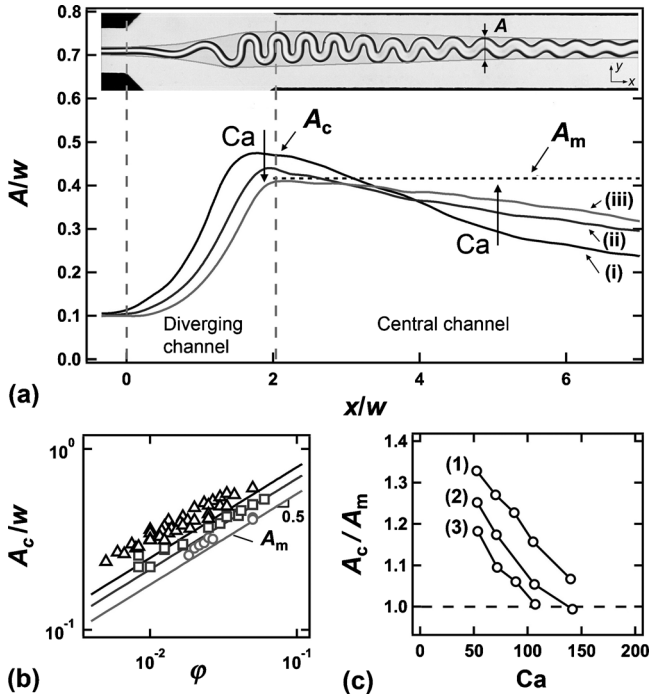

FIG. 9. Folding amplitude of capillary threads. (a) Influence of the capillary number Ca on the spatial evolution of A for $\varphi^{-1}=40$, $\chi=851$, Ca=53 (i), 106 (ii), and 142 (iii). Inset: micrograph with superimposed envelope amplitude corresponding to curve (iii). A_c corresponds to the capillary thread amplitude at the junction between the diverging and the central channel and A_m to the amplitude of a miscible fluid thread having the same χ. (b) Evolution of the maximum amplitude A_c as a function of the flow rate ratio φ for $\chi=170$ (○), 425 (□), and 851 (△). Solid line: corresponding miscible amplitude calculated from Eq. (1). Data for $\chi=4268$ have been omitted for clarity. (c) Influence of the capillary number Ca for $\chi=851$. Flow rate ratios, $\varphi=0.012(1), 0.025(2), 0.033(3)$.

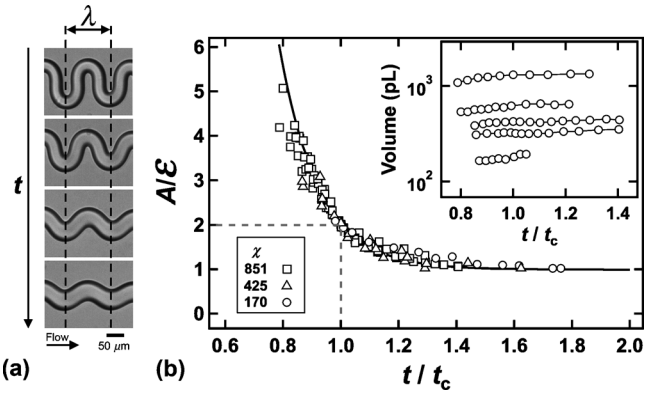

FIG. 10. Capillary stabilization of viscous threads. (a) Time-series of an individual fold: $\Delta t=16$ ms (fold reference frame), $\chi=851$, $Q_1=7$, and $Q_2=300$ μL/min. (b) Evolution of the amplitude-to-diameter ratio A/ε vs capillary time-scale t/t_c, $\chi=170$ (○), 425 (△), and 851 (□). Solid line: exponential fit $A/\varepsilon=1+c_0\exp(-c_1/t_c)$ with $c_0=1512$ and $c_1=7.25$. Inset: evolution of computed thread volume per wavelength.

=4865 cP). Therefore, capillary thread folding morphologies depend on both the capillary number Ca and the viscosity contrast χ.

In the central channel, the spatial period of folds λ increases linearly with the maximum amplitude A_c. The capillary wavelength λ remains fixed in the central channel and, for comparable χ, numerical values surpass those found for the miscible fluid case by nearly a factor of 2. In the diverging channel, the effect of interfacial tension on folds can qualitatively be understood by the fact that the production of larger folding amplitude A and larger wavelength λ allows for the generation of smaller interfacial areas. By contrast, in the central channel with parallel streamlines, as the wavelength λ remains fixed, capillary forces act by reducing A and thickening the thread diameter ε in order to conserve mass.

B. Capillary unfolding

Over time, capillary threads unfold in the central channel. High-speed imaging is used to monitor individual folds as they evolve when carried away in the surrounding fluid [Fig. 10(a)]. The morphological change due to interfacial tension γ_{12} consists in a reduction of the envelope amplitude A and an expansion of the thread diameter ε along the flow direction. The wavelength λ remains nearly constant during the process. For selected threads, the temporal evolution of A and ε is measured in Fig. 10(b). To compare threads having different viscosities η_1, time t is normalized by the viscous-capillary time-scale,[50] $t_c=\eta_1 h/\gamma_{12}$, which is calculated based on the channel height h. The reference time $t/t_c=1$ is arbitrarily chosen when $A/\varepsilon=2$ because this value is frequent in the experiment. Overall, data collapse on a single curve fit by $A/\varepsilon=1+c_0\exp(-c_1/t_c)$ with $c_0=1512$ and $c_1=7.25$. The exponential relaxation of a folded thread into a straight core occurs during a typical time $\tau\sim t_c$ for filaments having a relatively large amplitude-to-diameter ratio $A/\varepsilon\sim 5$.

The fact that λ remains constant during the relaxation process suggests that mass is conserved within a fold. To verify this assumption, the apparent area $A_a(t)$ of a fold is extracted. For a folded cylinder of uniform diameter ε, the apparent area $A_a=\varepsilon S$, where S is the length of the fold centerline, and the volume of a fold can be estimated as $V\approx\pi A_a\varepsilon/4$ [Fig. 10(b) inset]. Over the range of folds investigated, the calculated volume is found to remain constant, which supports the mass conservation argument. Theoretical and numerical examinations are needed to fully elucidate the influence of the motion of the interface on the "internal" flow of $L1$ within the thread.

C. Capillary arc-length

The evolution of the arc-length $s(x)$ of a capillary thread is determined in a fashion similar to the case of a miscible fluid thread. The thread centerline is initially distorted by the folding instability in the diverging channel $(x/w<2)$ and straightens in the central channel $(x/w>2)$ due to capillary effects [Fig. 11(a)]. The arc-length $s(x)$ increases sharply in the second part of the diverging channel $(x/w>1)$ and adopts a slope closer to unity in the central channel. Together with the maximum amplitude A_c, the mean thread corrugation ds/dx reaches a maximum value near the entrance of the central channel and smoothly decreases during the unfolding process [Fig. 11(b)]. In this typical example, the maximum corrugation remains approximately constant and the rate of fold damping decreases when the capillary number Ca increases.

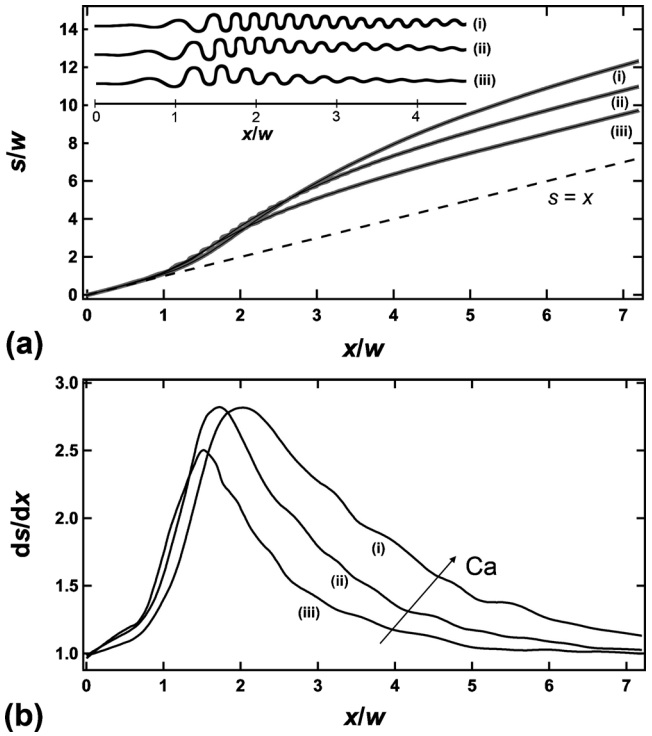

FIG. 11. Arc-length of capillary threads. (a) Spatial evolution of thread arc-length s for fixed $\varphi=0.01$ and $\chi=851$, Ca=87 (i), 70 (ii), and 52 (iii). Inset: corresponding digitally thicken thread centerlines. (b) Spatial evolution of the thread corrugation ds/dx for different capillary numbers Ca.

D. Shape instability

High-viscosity capillary threads ($\eta_1=4865$ cP) having large folding amplitudes A are subjected to a peculiar shape instability (Fig. 12). The flow morphology evolves from a folding pattern (which is essentially two-dimensional) to a coiling-like pattern characterized by an apparent helical thread motion. The system can be seen as implementing this mechanism as a strategy to rapidly reduce interfacial area. Indeed, the time-scale τ over which the buckling amplitude diminishes is about an order of magnitude smaller than the capillary time-scale t_c. Another major difference with the capillary unfolding mechanism is the nearly constant thread diameter ε in the regions between bends. The growth of bulbs in the bending zones suggests a local accumulation of the fluid collected from the diminution in the thread arc-length during the amplitude reduction process. This phenomenon illustrates the complex and unexpected interplay between buckling instabilities and multiphase flows in microgeometries.

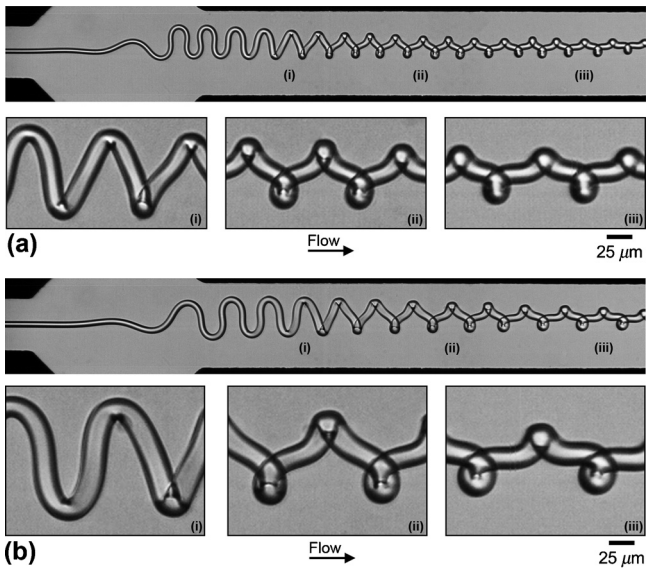

FIG. 12. Shape instability of highly viscous-capillary threads $\chi=4344$ (flow rates in μL/min): (a) $Q_1=2$, $Q_2=600$ and (b) $Q_1=5$, $Q_2=800$. Transition from folding to coiling is shown with enlarged micrographs along the flow direction.

V. CONCLUSION

In this paper, viscous buckling instabilities are used to build regular and elaborated fluid microstructures. The influence of fluid physicochemical properties (such as viscosity and interfacial tension) on microfluidic multiphase flows is discussed. Methods for determining the morphology of threads are developed using scaling laws based on viscosity contrast χ, flow rate ratio φ, and capillary number Ca. A variety of original flow regimes are identified and examined.

The radial increase of a viscous thread in a diverging microchannel is quantified using a thread dilation factor σ. Experiments suggest that for both miscible and immiscible fluid threads, $\sigma\sim\chi^{-1/2}$. For miscible fluid threads, the measured amplitude A of the folding envelope in the central channel is in good agreement with the theory of folding of viscous sheets falling onto a surface in air. In the case of a viscous microenvironment and in the absence of impinging surfaces, our findings show that $A\sim\chi^{1/4}\varphi^{1/2}$. The folding amplitude of capillary threads in the central channel follows a similar scaling when the capillary number $\mathrm{Ca}\to\infty$. For a wide range of viscosity contrast χ, the shapes of miscible fluid folds are classified on a single phase-diagram. Distinct regions are identified for small ($\chi\leq 10^2$), moderate (χ ranges between 10^2 and 10^3), and large viscosity contrasts ($\chi\geq 10^3$). Analysis of the evolution of the thread arc-length-to-wavelength ratio S/λ reveals that the filament maximal corrugation occurs for moderate viscosity contrasts. In this case, the wavelength of folding λ is directly proportional to the envelope amplitude A. Investigations with immiscible fluid threads showed that the viscous folding instability is significantly inhibited when the capillary number $\mathrm{Ca}\leq 14$. The phenomenon of capillary unfolding where a corrugated thread straightens over time is demonstrated. In particular, we show that the viscous-capillary time-scale $t_c=\eta_1 h/\gamma_{12}$ controls the decay of the amplitude-to-thickness ratio A/ε of such threads. Finally, we report a flow regime for high-viscosity capillary threads that consists of a smooth spatial transition from unfolding to "uncoiling."

This work provides a direct experimental evaluation of miscible and immiscible fluid dynamics in microfluidic systems. Focus is given on the sinuous modes of deformation of fluid threads. We experimentally confirm that such perturbations are amplified by viscous forces and damped by capillary forces. This situation, which we refer to as "viscous instability," is complementary to the well-known "capillary

instability" where varicose perturbations are enhanced by capillary forces and reduced by viscous forces. Although our experimental approach to this problem quantifies the influence of interfacial and bulk fluid properties on viscous microfolds, it also highlights the need for theoretical and computational treatments of these phenomena in the context of multiphase flows. Our study provides new capabilities for dynamically structuring high-viscosity fluids into very regular micropatterns that can be precisely adjusted. In general, elucidating the basic interactions between viscous streams in confined geometries is important for improving manipulations of highly viscous fluids (such as heavy oils) with solvents in continuous reactors.

ACKNOWLEDGMENTS

This material is based upon the work supported by the National Science Foundation under Grant No. CBET-0932925.

[1]H. A. Stone, A. D. Stroock, and A. Ajdari, "Engineering flows in small devices: Microfluidics toward a lab-on-a-chip," Annu. Rev. Fluid Mech. **36**, 381 (2004).
[2]T. M. Squires and S. R. Quake, "Microfluidics: Fluid physics at the nanoliter scale," Rev. Mod. Phys. **77**, 977 (2005).
[3]A. A. Darhuber and S. M. Troain, "Principle of microfluidic actuation by modulation of surface stresses," Annu. Rev. Fluid Mech. **37**, 425 (2005).
[4]P. Garstecki, M. Fuerstman, H. A. Stone, and G. W. Whitesides, "Formation of droplets and bubbles in a microfluidic T-junction-scaling and mechanism of breakup," Lab Chip **6**, 437 (2006).
[5]S. Y. Teh, R. Lin, L. H. Hung, and A. P. Lee, "Droplet microfluidics," Lab Chip **8**, 198 (2008).
[6]A. Günther, M. Jhunjhunwala, M. Thalmann, M. A. Schimdt, and K. F. Jensen, "Micromixing of miscible liquids in segmented gas-liquid flow," Langmuir **21**, 1547 (2005).
[7]H. Song, D. L. Chen, and R. F. Ismagilov, "Reactions in droplets in microfluidic channels," Angew. Chem., Int. Ed. **45**, 7336 (2006).
[8]C. N. Baroud, M. R. de Saint Vincent, and J. P. Delville, "An optical toolbox for total control of droplet microfluidics," Lab Chip **7**, 1029 (2007).
[9]S. Park, M. A. Teitell, and P. Y. Chiou, "Single-sided continuous optoelectrowetting (SCOEW) for droplet manipulation with light pattern," Lab Chip **10**, 1655 (2010).
[10]S. Tomotika, "On the instability of a cylindrical thread of a viscous liquid surrounded by another viscous fluid," Proc. R. Soc. London, Ser. A **146**, 322 (1935).
[11]D. T. Papageorgiou, "On the breakup of viscous liquid threads," Phys. Fluids **7**, 1529 (1995).
[12]L. E. Johns and R. Narayanan, *Interfacial Instability* (Springer-Verlag, New York, 2002).
[13]P. G. Drazin and W. H. Reid, *Hydrodynamic Stability* (Cambridge University Press, Cambridge, 2004).
[14]G. M. Homsy, "Viscous fingering in porous media," Annu. Rev. Fluid Mech. **19**, 271 (1987).
[15]E. Lajeunesse, J. Martin, N. Rakotomalala, D. Salin, and Y. C. Yortsos, "Miscible displacement in a Hele-Shaw cell at high rates," J. Fluid Mech. **398**, 299 (1999).
[16]R. Balasubramaniam, N. Rashidnia, T. Maxworthy, and J. Kuang, "Instability of miscible interfaces in a cylindrical tube," Phys. Fluids **17**, 052103 (2005).
[17]T. Cubaud and T. G. Mason, "Folding of viscous threads in diverging microchannels," Phys. Rev. Lett. **96**, 114501 (2006).
[18]L. D. Landau and E. M. Lifshitz, *Theory of Elasticity* (Pergamon, Oxford, 1986).
[19]J. Teichman and L. Mahadevan, "The viscous catenary," J. Fluid Mech. **478**, 71 (2003).
[20]J. P. Koulakis, C. D. Mitescu, F. Brochard-Wyart, P. G. de Gennes, and E. Guyon, "The viscous catenary revisited: Experiments and theory," J. Fluid Mech. **609**, 87 (2008).
[21]A. Boudaoud and S. Chaïeb, "Singular thin viscous sheet," Phys. Rev. E **64**, 050601(R) (2001).
[22]G. Debrégeas, P. G. de Gennes, and F. Brochard-Wyart, "The life and death of "bare" viscous bubbles," Science **279**, 1704 (1998).
[23]R. da Silveira, S. Chaïeb, and L. Mahadevan, "Rippling instability of a collapsing bubble," Science **287**, 1468 (2000).
[24]J. O. Cruickshank and B. R. Munson, "Viscous fluid buckling of plane and axisymmetric jets," J. Fluid Mech. **113**, 221 (1981).
[25]R. W. Griffiths and J. S. Turner, "Folding of viscous plumes impinging on a density or viscosity interface," Geophys. J. **95**, 397 (1988).
[26]L. Mahadevan, W. S. Ryu, and A. D. T. Samuel, "Fluid 'rope trick' investigated," Nature (London) **392**, 140 (1998).
[27]L. Mahadevan, W. S. Ryu, and A. D. T. Samuel, "Correction: Fluid 'rope trick' investigated," Nature (London) **403**, 502 (2000).
[28]M. Maleki, M. Habibi, R. Golestanian, N. M. Ribe, and D. Bonn, "Liquid rope coiling on a solid surface," Phys. Rev. Lett. **93**, 214502 (2004).
[29]N. M. Ribe, J. R. Lister, and S. Chiu-Webster, "Stability of a dragged viscous thread: Onset of "stitching" in a fluid mechanical "sewing machine"," Phys. Fluids **18**, 124105 (2006).
[30]B. Pouligny and M. Chassande-Mottin, "Air ingestion by a buckled viscous jet of silicone oil impacting the free surface of the same liquid," Phys. Rev. Lett. **100**, 154501 (2008).
[31]S. Nagahiro and Y. Hayakawa, "Bending-filament model for buckling and coiling instability of a viscous fluid rope," Phys. Rev. E **78**, 025302(R) (2008).
[32]E. H. T. Whitten, *Structural Geology of Folded Rocks* (Rand McNally, Chicago, 1966).
[33]A. M. Johnson, *Styles of Folding* (Elsevier, Amsterdam, 1977).
[34]P. J. Hudleston and L. Lan, "Information from fold shapes," J. Struct. Geol. **15**, 253 (1993).
[35]N. M. Ribe, "Periodic folding of viscous sheets," Phys. Rev. E **68**, 036305 (2003).
[36]N. M. Ribe, E. Stutzmann, Y. Ren, and R. van der Hilst, "Buckling instabilities of subducted lithosphere beneath the transition zone," Earth Planet. Sci. Lett. **254**, 173 (2007).
[37]A. M. Johnson and R. C. Fletcher, *Folding of Viscous Layers* (Columbia University Press, New York, 1994).
[38]T. Cubaud and T. G. Mason, "Capillary threads and viscous droplets in square microchannels," Phys. Fluids **20**, 053302 (2008).
[39]T. Cubaud and T. G. Mason, "High-viscosity fluid threads in weakly diffusive microfluidic systems," New J. Phys. **11**, 075029 (2009).
[40]C. Chung, D. Choi, J. M. Kim, K. H. Ahn, and S. J. Lee, "Numerical and experimental studies on the viscous folding in diverging microchannels," Microfluid. Nanofluid. **8**, 767 (2010).
[41]T. Cubaud and T. G. Mason, "Formation of miscible fluid microstructures by hydrodynamic focusing in plane geometries," Phys. Rev. E **78**, 056308 (2008).
[42]J. O. Cruickshank and B. R. Munson, "An energy loss coefficient in fluid buckling," Phys. Fluids **25**, 1935 (1982).
[43]T. Cubaud and C.-M. Ho, "Transport of bubbles in square microchannels," Phys. Fluids **16**, 4575 (2004).
[44]IMAGEJ is a public domain Java image processing program. The source code is freely available (at http://rsb.info.nih.gov/ij/ as of March 2011). The author, Wayne Rasband, is at the Research Services Branch, National Institute of Mental Health, Bethesda, Maryland, USA (at wayne@codon.nih.gov as of March 2011).
[45]S. C. R. Dennis, W. H. H. Banks, P. G. Drazin, and M. B. Zaturska, "Flow along a diverging channel," J. Fluid Mech. **336**, 183 (1997).
[46]P. G. Drazin, "Flow through a diverging channel: Instability and bifurcation," Fluid Dyn. Res. **24**, 321 (1999).
[47]V. Putkaradze and P. Vorobieff, "Instabilities, bifurcations, and multiple solutions in expanding channel flows," Phys. Rev. Lett. **97**, 144502 (2006).
[48]M. Skorobogatiy and L. Mahadevan, "Folding of viscous sheets and filaments," Europhys. Lett. **52**, 532 (2000).
[49]N. Rashidnia, R. Balasubramaniam, and D. Del Signore, "Interfacial tension measurement of immiscible liquids using a capillary tube," AIChE J. **38**, 615 (1992).
[50]J. Eggers, "Nonlinear dynamics and breakup of free-surface flows," Rev. Mod. Phys. **69**, 865 (1997).